New reflections on hard X-ray photon-in/photon-out spectroscopy

Sara Lafuerza[1], Marius Retegan[1], Blanka Detlefs[1], Ruchira Chatterjee[2], Vittal Yachandra[2], Junko Yano[2] and Pieter Glatzel[1,*]

[1]European Synchrotron Radiation Facility, 71 Avenue des Martyres, 38000 Grenoble, France

[2]Molecular Biophysics and Integrated Bioimaging Division, Lawrence Berkeley National Laboratory,
1 Cyclotron Road, Berkeley, CA 94704, USA

***glatzel@esrf.fr**

Abstract

Analysis of the electronic structure and local coordination of an element is an important aspect in the study of the chemical and physical properties of materials. This is particularly relevant at the nanoscale where new phases of matter may emerge below a critical size. X-ray emission spectroscopy (XES) at synchrotron radiation sources and free electron lasers has enriched the field of X-ray spectroscopy. The spectroscopic techniques derived from the combination of X-ray absorption and emission spectroscopy (XAS-XES), such as resonant inelastic X-ray scattering (RIXS) and high energy resolution fluorescence detected (HERFD) XAS, are an ideal tool for the study of nanomaterials. New installations and beamline upgrades now often include wavelength dispersive instruments for the analysis of the emitted X-rays. With the growing use of XAS-XES, scientists are learning about the possibilities and pitfalls. We discuss some experimental aspects, assess the feasibility of measuring weak fluorescence lines in dilute, radiation sensitive samples, and present new experimental approaches for studying magnetic properties of colloidal nanoparticles directly in the liquid phase.

Introduction

X-ray spectroscopy can provide the energy and the transition probabilities to the excited states of the electronic Hamiltonian. X-ray absorption arises from a transition from an inner-shell atomic orbital to an unoccupied bound orbital or into the continuum and X-ray emission occurs when an inner-shell vacancy is filled by an electron from a shallower inner-shell atomic or valence orbital.[1,2] The two processes are combined in photon-in/photon-out (PIPO) spectroscopy that provides rich information on the electronic structure and thus the coordination environment of an element (the analyte). A growing number of experimental stations[3–18] at synchrotron radiation sources and free electron lasers around the world provide researchers in all fields of natural sciences with the tools to explore the possibilities of PIPO spectroscopy. Photon-out X-ray emission or X-ray fluorescence spectroscopy using laboratory X-ray sources, particle impact or radioactive isotopes, realized with wavelength dispersive emission spectrometers with energy bandwidth around 1 eV is being re-discovered because of commercial instruments that are nowadays available. Interestingly, this development was to some extent triggered by synchrotron radiation sources that allowed the study of resonant inelastic X-ray scattering (RIXS) because of the tuneable and brilliant X-ray source. The efforts that went into the development of instruments for RIXS now also materialize in state-of-the-art laboratory instruments for X-ray emission spectroscopy (XES). XES instruments developed in the last years include both point-to-point scanning[19–21] and dispersive von Hámos [22–24] as well as superconducting micro-calorimeter spectrometers.[25]

The incoming energy in X-ray absorption spectroscopy (XAS) is given by the absorption edge and a beamline that is optimized for XAS thus ideally covers a large energy range continuously. Figure 1 shows the calculated flux at the ESRF (6 GeV, 200 mA) for a given configuration of undulators and slits. The high electron energy allows covering an energy range from 2 to well above 25 keV continuously with high photon flux. The installation of revolver undulators that allow operation with two different periods increases the flux and the energy range where the undulator fundamental and third harmonic can be used. An important development will be new vacuum chambers with reduced minimal undulator gaps that will increase the energy range for a given period and harmonic and thus increase the photon flux.

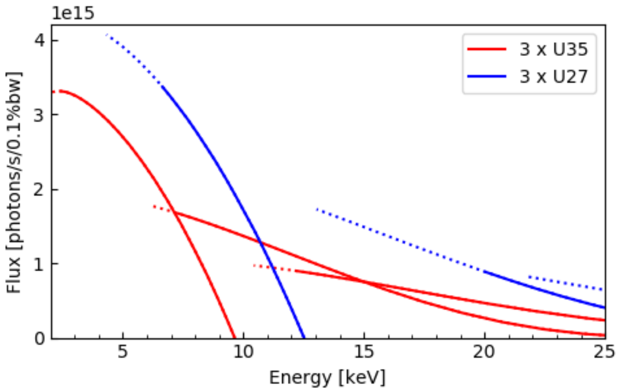

*Figure 1 Calculated flux through an 1.5 mm x 1.0 mm (horizontal x vertical) aperture at 30 m from the source for a revolving undulator (35 and 27 mm period) of total length 4.8 m (segmented into 3 * 1.6 m assuming perfect phasing between the undulators and 200 mA ring current). The dotted lines show the increase in range when decreasing the minimal gap from 11.2 to 9 mm. The different ranges for each period show the fundamental, 3rd and 5th harmonic.*

The field of PIPO has grown enormously over the past decades and it is important to limit the scope of this paper. RIXS has become a powerful tool for the study of collective excitations that emerge from the long range order in solid state systems.[5,26] Here, the dependence of the spectroscopic signal on the magnitude and direction of the momentum transfer is an important information. We address here experiments without macroscopic ordering of the atomic structure with respect to the X-ray beam (excluding magnetic moments, see below for X-ray magnetic circular dichroism) and the dependence on the momentum transfer is partly averaged or simply ignored because it would be too complex to consider it accurately. Our focus is on hard X-ray XAS-XES spectroscopy recorded with a wavelength dispersive instrument with energy bandwidth around 1 eV. The X-ray absorption near edge structure (XANES) signal shows a spectral sharpening effect when recorded in fluorescence mode using such an instrument. The high energy resolution fluorescence detected (HERFD) XANES spectroscopy has become a very popular tool to extract more information from the spectra.[2,6,27–30] We furthermore discuss RIXS with absorption into the K pre-edge of a 3*d* transition metal combined with X-ray magnetic circular dichroism (RIXS-MCD), a novel magnetospectroscopy that is gaining attention for the characterization of magnetic nanomaterials.

We address in the following some experimental aspects that become increasingly important with the multiplying use of PIPO at high brilliance X-ray sources. These are radiation damage and the resulting limits of experimental feasibility, spectral distortions due to over-absorption, a new approach for range-extended XAS, and the influence of the emission energy choice in HERFD-XANES. The final section presents examples for the study of colloidal nanoparticles where the hard X-ray probe greatly facilitates the experimental procedure. We consider this article a continuation of our previous publications that discuss general aspects of XAS-XES.[1,2]

Radiation-sensitive samples

The higher photon densities that will become accessible with the newly available extremely brilliant source (EBS) at the ESRF beamlines, make the problem of radiation damage even more pertinent. While the topic of radiation damage has been thoroughly discussed and documented by the community of macromolecular crystallographers[31], the topic is much less a matter of research elsewhere. In X-ray spectroscopy, a number of studies reported on beam damage effects.[32–48] Dose limits may vary considerably depending on the type of sample and the technique used to characterize the damage. Mitigation strategies may concern the sample preparation and conditions during measurements, X-ray characteristic (energy, pulse duration), data treatment, but also improvements of the X-ray detection chain. PIPO is a photon-hungry technique. The detection efficiency is low mainly because of the small fraction of a sphere that is captured even by the latest generation of instruments (tens of milisteradians).[6,12,49,50] Many of the most interesting X-ray emission lines are furthermore weak, e.g. the valence-to-core lines.[51–53] The count rates in a PIPO experiment may be as low as a few tens of Hz with at an incoming photon flux of 10^{13} Hz. Damage of the sample under the X-ray beam utterly changes the experimental strategy and may even render an experiment impossible.

Experimental protocols must be adapted for radiation sensitive samples. The X-ray beam must frequently hit fresh spots of the sample. Dispersive (e.g. von Hámos) XES instruments offer a great advantage here as the entire spectrum is acquired in a single-shot without scanning, and the sample can thus be moved under the beam during data acquisition. Non-dispersive instruments may still be the preferred choice for other reasons[17] and are also used for radiation sensitive samples. Ideally, one records a full spectrum on the same beam spot on the sample because variations of the analyte concentration across the sample will create artefacts. However, acquisition times per data point below a certain limit (e.g. 1 second) will render the measurement increasingly inefficient because of dead time for motor motions. Continuous (on-the-fly) scans may be an alternative but are challenging to implement for XES in particular for multi-crystal spectrometers because a large number of motors have to move in a precisely synchronized fashion. Figure 2 shows an Fe Kβ XES spectrum of Fe in green rust[54] where each point was recorded on a different spot with 1 second acquisition time, *i.e.* below the acceptable dose limit. After the full scan is completed, each beam position on the sample is revisited and the count rate in the maximum of the $K\beta_{1,3}$ line is recorded in a second scan. The final Kβ spectrum (blue line in Figure 2) is obtained by normalizing the first scan (red line in Figure 2) to the incoming flux and the flux-normalized signal of the second scan. Figure 2 shows that this is a viable approach to record data in radiation sensitive samples.

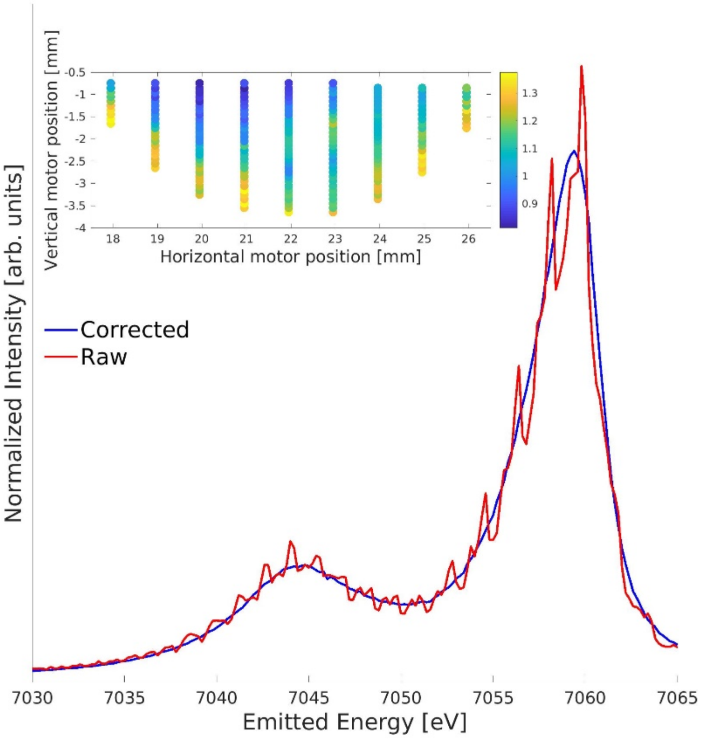

Figure 2 $K\beta$ lines of Fe in green rust.[54] *Each data point was recorded with the beam on a different position on the sample. The spectrum is shown before (red) and after (blue) correction for the Fe $K\beta_{1,3}$ maximum signal from each spot. Both spectra are normalized to the incoming flux. The inset shows the variation of the Fe $K\beta_{1,3}$ maximum signal across the sample.*

Another strategy frequently adopted to prevent radiation damage in samples in solution is the use of a liquid jet setup where the X-ray beam hits an uncontained jet. The analyte is homogeneously distributed thus preventing signal variations as observed for solid samples scanned under the beam. In this way, a large sample volume is used in a single scan. However, even if this caution is taken, in some cases the sample may still show beam modulation effects. We show an example for Fe^{3+} in water solution, which is not stable under the X-ray beam. Figure 3 shows Fe K edge HERFD-XANES data as a function of the elapsed time, measured on Fe^{3+} and Fe^{2+} ions in water solution circulating in a liquid jet setup previously described elsewhere.[30] In this system, a liquid jet of 1 mm diameter is cycled through the X-ray beam, which shines on the uncontained jet exposed to air. The jet speed was 100 ml/min and the beam size was about 100 x 500 (vertical x horizontal) μm^2. $[Fe(H_2O)^6]^{3+}$ and $[Fe(H_2O)^6]^{2+}$ complexes in 50 ml solution were prepared by dissolving $Fe(NO_3)_3{\cdot}9H_2O$ and $FeSO_4{\cdot}7H_2O$ salts respectively, in deionized water to get a concentration of 0.1 M at pH ≈ 1.[55,56] While Fe^{2+} in solution appears stable in the beam, Fe^{3+} in solution shows photoreduction effect towards Fe^{2+} over time. Recently, photoreduction of Fe^{3+} in solution was also reported in measurements at 12 K in a cryostat.[57] It seems that Fe^{3+} in solution is highly unstable under the X-rays and immediately after a sample portion is illuminated, photoreduction starts to develop and spreads over the remaining sample.

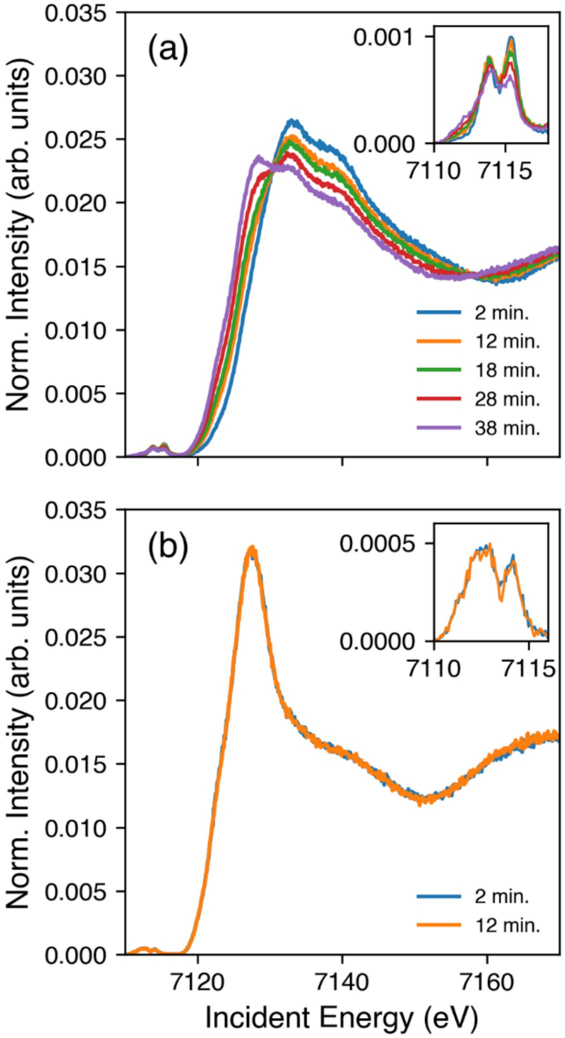

Figure 3 Stability of Fe ions in solution under the X-ray beam measured in a liquid jet setup. Kα$_1$-detected Fe K edge HERFD-XANES of (a) Fe^{3+} and (b) Fe^{2+} ions are displayed as a function of the elapsed time. The insets show a zoom in the pre-edge region.

Moving a solid sample under the beam (Figure 2) only provides good results if the signal is dominated by the analyte fluorescence line. This may not be the case in e.g. valence-to-core (vtc) XES in dilute systems where non-resonant Compton and Raman scattering strongly contribute to the signal. Their contribution depends on the incoming and emission energy and the beam position on the sample, i.e. the ratio between fluorescence signal and background varies as a function of emission energy and beam position. A second scan to obtain a map of the analyte signal strength as previously described can therefore not be used to correct for the variation in the fluorescence signal that arises from moving the sample under the beam. In this case, one can choose to omit the normalization to the varying signal across the sample and instead average over dozens or even hundreds of scans, i.e. positions of the beam on the sample. It appears a reasonable assumption that the signal variation over the spectral range due to different analyte signal strength decreases with the number of measured samples if there are no systematic errors. To ensure this, all motor positions that are used to displace the sample under the beam must yield identical experimental conditions. For example, one must avoid hitting the sample holder as this would increase the background signal and the relation between emission energy and motor positions should be scrambled. This protocol was used to record vtc XES of Mn in PS II (see below).

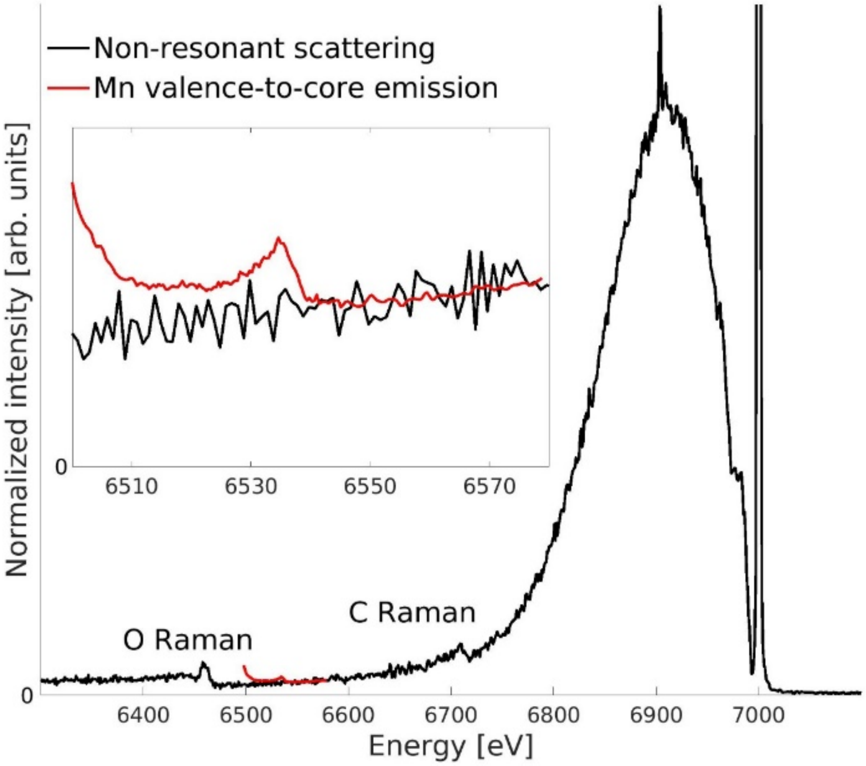

Figure 4 Non-resonant X-ray scattering (black) and vtc XES of Mn in the protein complex photosystem-II (red). The spectra are only normalized to the incoming flux. The non-resonant spectrum was recorded on ice with the emission energy set to 6580 eV and the incident energy scanned between 6500 and 7200 eV. It was inverted and shifted to have the elastic peak at 7000 eV. The Mn vtc spectrum of PS II was recorded with incoming energy at 7000 eV. The acquisition time per data point is 0.5 seconds in the non-resonant spectrum and 56 seconds in the Mn vtc spectrum. Both spectra were recorded under identical conditions (see Figure 6).

Figure 4 illustrates the challenges when recording vtc spectra in samples with low analyte concentration. The weak fluorescence signal sits on a large background arising from non-resonant scattering. The incoming energy should be chosen well above the K absorption edge to avoid undesired resonance effects. It should also be lower than the energy it requires to simultaneously ionize the K and L shell (KL edge) whose energy can be estimated by adding the L edge of the Z+1 element to the K edge energy of the analyte, e.g. E(Mn K edge) + E(Fe L edge) = 7250 eV.[58] The KLβ emission lines are on the high energy side of the vtc lines and may render an analysis more complicated.[58] In the energy window between K and KL edge one would like to minimize the background from non-resonant scattering (Compton, Raman). In the example in Figure 4 we chose 7000 eV as excitation energy. The sample is a frozen solution of the protein complex photosystem II (PS II) with Mn concentration of ~ 0.9 mM.[59] The background is about 3 times as strong as the signal. The intensity of the non-resonant signal scales with $\cos^2$ of the horizontal scattering angle with linear polarized synchrotron radiation while the fluorescence signal is isotropic for a solution. Thus, one would like the XES suspended solid angle as large as possible but close to 90 degrees, and a compromise has to be found between detection efficiency and signal to background ratio.

Estimating the required total counts

The count rates for a given sample, incoming flux, and emission spectrometer can be predicted quite accurately which is important to assess the feasibility of an experiment.[60] XES is generally recorded in single photon detection and the spectral error is given by Poisson statistics. If a radiation damage study gives a maximal acceptable dose, one can determine the amount of sample that is necessary to achieve a certain statistical error. Often, the crucial unknown quantity is the spectral change between two species that one aims to identify in the systems under study. We can analyse the difference spectrum normalized to the spectral counts. Ideally, two species give fully separated spectral features. This would correspond to the spectral difference of 1. In most cases, the spectral features overlap and the spectral difference may only be as strong as 10 %. One then needs to define if simply detecting a spectral difference suffices or whether a more precise spectral analysis is necessary. The former may be sufficient in some studies while often the difference spectrum requires a small error bar e.g. for comparison with theoretical spectra. Either way, the required counts scale with the square of the spectral difference.[60] We discuss it in the following an example.

Valence-to-core XES is a valuable tool to track changes in the ligand environment of metal centers in catalytic systems. For example, the manganese atoms in the oxygen-evolving complex of PS II cycle through different oxidation states to provide the required electrons for the water-splitting reaction.[61] In such systems, low analyte concentration, sample sensitivity, and considerable background due to secondary decay processes can lead to very long acquisition times. In the following, we present an estimation of the counts required to have a statistically significant difference signal between two states of the PS II catalytic cycle. We have employed an approach presented previously for the evaluation of required counts in dichroism and pump-and-probe experiments.[60] For completeness, we briefly illustrate the derivation of the formula given in the previous reference. We define the signal to noise ratio (SNR) for each spectral point as the ratio between the average signal and the standard deviation. Here we are interested in the difference signals and we can rewrite the signal to noise equation as:

$$s = \frac{C_f - C_g}{\sqrt{C_f + C_g}} \cong \frac{C_f - C_g}{\sqrt{2C_g}}$$

where the denominator is the standard deviation resulting from two processes that follow Poisson statistics. In this case, C_g are the counts in the ground or initial state, while C_f are the counts after one flash. It is well established that only a fraction of the catalytic centers advance from one catalytic state to the next, and therefore the counts after one flash are:

$$C_f = fC_e + (1 - f) \cdot C_g$$

where C_e are the counts in the pure, excited state, which we can couple to the counts in the ground state via the relative change parameter defined as:

$$r = \frac{C_e - C_g}{C_g}$$

The required counts in the ground state are then:

$$C_g = 2\frac{s^2}{(fr)^2}$$

The equation can of course also be used for the comparison of pure spectra with f=1. We apply the equation to determine the required counts (C_g) in the S_1 dark stable state of PSII. Upon flash illumination, the system advances to the S_2 state with one of the manganese atoms changing its oxidation state from Mn(III) to Mn(IV).[62] The fraction of centers that advance from S_1 to S_2 depends on many experimental factors. In the following, we assume $f = 0.9$, which is probably an upper limit. We determined the relative change from the theoretical vtc spectra of the two states calculated using the previously published structural models and protocols (Figure 5).[62,63] At the maximum of the S_1 state, the relative change was 0.02. If we require an SNR to be 2, then the required counts at the maximum of the S_1 state will be approximately 24 700. In this case, the number of required counts is large, mainly due to the small relative change. This might be surprising, but not completely unexpected, as in the present case only one metal center changes oxidation state while all of them contribute to the total vtc spectrum.

In the previous discussion, we have not considered the background due to Compton or Raman processes. To include it, we need to change the starting SNR equation. In the following, we assume that the background is identical in both measurements and that it is proportional to the signal, with a proportionality factor n.

$$s = \frac{C_f - C_g}{\sqrt{C_f + C_g + 2B}} \cong \frac{C_f - C_g}{\sqrt{2C_g + 2B}} = \frac{C_f - C_g}{\sqrt{2(1+n)C_g}}$$

The final equation for the required counts then becomes:

$$C_g = 2(n+1)\frac{s^2}{(fr)^2}$$

For the PSII vtc XES measurements, the background is approximately three times larger than the actual signal. In this case the number of required counts to get a statistically significant difference increases by a factor of 4 to about 98 800.

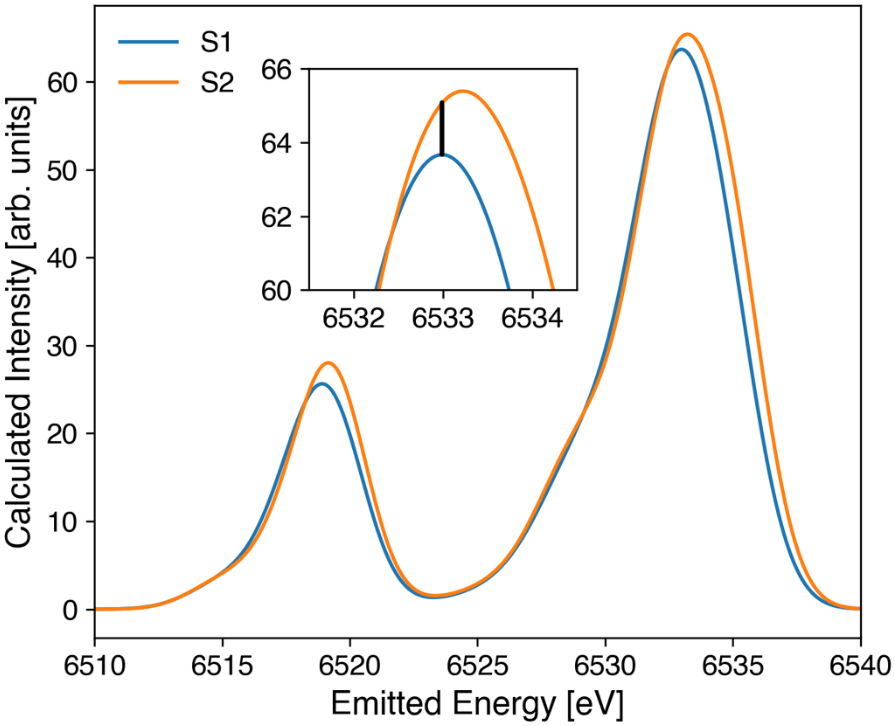

Figure 5 Calculated Mn vtc XES spectra for the S_1 and S_2 state of PSII. The differences between the states at the maximum of the S_1 spectrum is indicated in the inset with a vertical black line.

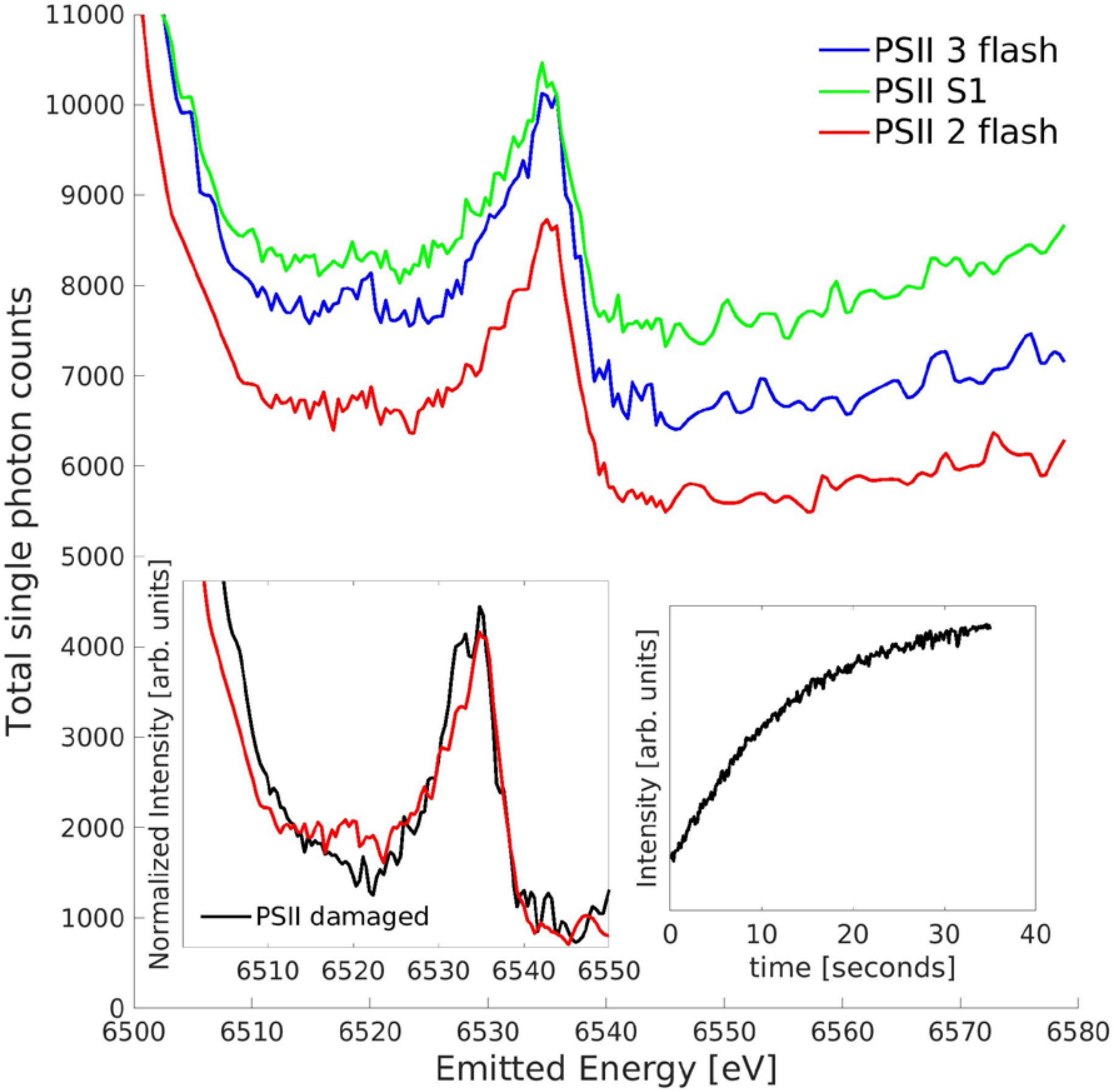

Figure 6 Mn vtc XES of PSII. Spectra are shown for the dark-adapted state S1 and flash illuminated samples. The Mn concentration was ~0.9 mM and the sample thickness ~ 0.8 mm. For more details on the sample preparation see[64]*. The spectra were recorded using 5 spherical analyser crystals (Si (440), R=1000m, r=100mm) with the central crystal at 90 degrees horizontal scattering angle. The beam size was 0.7 x 0.1 mm*^{2} *(horizontal x vertical) and the total flux 2*10*^{13} *photons/second. The acquisition time per beam spot on the sample was 2 seconds and the count rate in the maximum of the* $K\beta_{2,5}$ *line was ~15 Hz on a background of ~45 Hz. The left inset shows a comparison between the 2 flash PSII sample and a strongly damaged sample. The right inset shows the evolution of the intensity of the* $K\beta_{1,3}$ *line as a function of time, i.e. with increasing dose (uncalibrated emission energy = 6492.8 eV with the maximum of* $K\beta_{1,3}$ *= 6491.6 eV for intact PS II; the incoming energy was 7000 eV). All spectra were recorded at 20 K in a He atmosphere >300mbar.*

Figure 6 shows the Mn vtc XES lines of PS II in the dark-adapted state S_1 and advanced by 2 and 3 flashes. The total counts accomplished in the data is between 7000 and 10000 which is not sufficient to establish spectral differences in agreement with our estimate. A comparison with a strongly X-ray damaged sample (left inset Figure 6) does allow to identify spectral differences because the relative change parameter r is larger as the Mn ions are removed from their environment in the oxygen evolving complex.[40] The time evolution of the X-ray damage can be monitored by recording the spectral intensity at fixed emission energy as a function of time. Figure 6 right inset shows an increase of the XES spectral intensity when the emission energy is tuned to the high energy side of the $K\beta_{1,3}$ maximum of intact PS II consistent with a reduction of Mn.[65] The photon density was $3*10^8$ photons/second/μm and the sample is fully reduced after 40 seconds. Photon densities three to four orders of magnitude higher than in the present study are common at spectroscopy beamlines around the world. Under such conditions it would be challenging to even observe the X-ray damage.

Modulation of the sample under an X-ray beam is not always unwanted. Desired effects of X-rays can be local changes of the conductivity,[66] emulating the effects of heavy ion impact and combining cause with diagnose when X-rays reproduce modifications that are otherwise achieved using optical or thermal excitations.[67] We show in Figure 7 an example for Eu in $BaMgAl_{10}O_{17}$. In its oxidation state II, Eu luminesces in the blue and it can be excited by UV light and X-rays. Degradation of the luminescence properties of $BaMgAl_{10}O_{17}:Eu^{2+}$ (BAM:Eu^{2+}) was observed under prolonged UV-and X-ray illumination. Combining X-ray spectroscopy with a probe of the optical luminescence shows that the decrease in luminescence properties arises from oxidation of Eu while the atomic structure remains intact. Interestingly, a large percentage of Eu remains as Eu^{2+} in the system even when the luminescence intensity arising from Eu^{2+} has disappeared. A possible explanation invokes "killer" centers of a certain radius around oxidized Eu that prevent transfer of energy to Eu^{2+} to let it luminesce.[68]

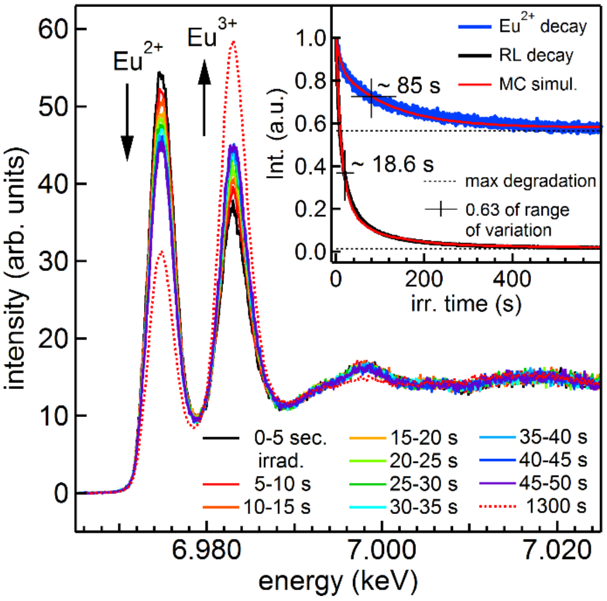

Figure 7 X-ray induced oxidation of Eu^{2+} observed in $L\alpha_1$-detected Eu L_3 edge HERFD-XANES on BAM:Eu. The inset shows the decay of Eu^{2+} XANES peak (blue) and of the integrated luminescence (black) during irradiation together with the results of a Monte Carlo (MC) simulation (red). Reprinted with permission from ref.[68] Copyright © 2017, American Chemical Society.

Following the previous considerations, the amount of sample that is required to render an analysis of the data statistically meaningful is given by the experimental setup. Cooling is the first measure to mitigate radiation damage and available at most experimental stations. However, often cooling does not sufficiently slow down the process of radiation damage or may not be desired or possible (e.g. *in situ* experiments). Thus, the most important path towards improving studies on radiation sensitive samples is to increase the captured solid angle. Despite the efforts made in the past, it appears that in view of the small fraction of a sphere currently covered by XES instruments, or fluorescence detected XAS in general for that matter, there is still considerable room for improvement.

Over-absorption

K. Hämäläinen used in 1991 an emission spectrometer to record the intensity of the $L_{\alpha 1}$ fluorescence line while scanning the incoming beam through the L_3 absorption edge of Dy. The result, compared to an absorption spectrum recorded in transmission mode, looked like a dramatically line sharpened absorption edge.[69] The technique has been named partial fluorescence yield (PFY), high energy resolution fluorescence detected (HERFD) or simply high resolution (HR) XAS. The present authors prefer HERFD-XAS for reasons explained elsewhere.[2] It was subsequently pointed out by several authors that a spectrum recorded in such a way does not measure a signal that is necessarily proportional to the photoelectric absorption coefficient.[70] This is often not a concern, e.g. when spectral evolutions as a function of an external stimulus are recorded or when the data analysis is based on the comparison with model compounds that are measured in an identical fashion. Furthermore, it is possible to calculate a HERFD-XAS spectrum using the theoretical formalism of RIXS, i.e. the resonant Kramers-Heisenberg equation.

HERFD-XAS not only yields sharper spectral features but also suppresses the background arising from unwanted X-ray events such as those originating in the matrix. As the energy resolution is achieved using wavelength dispersive optics there are few constraints on the detector which allows optimizing the linear response. This leads to excellent data quality in HERFD-XAS, which is offered at an increasing number of experimental stations.

An important problem in HERFD-XAS is that it uses fluorescence detection (another reason we prefer this acronym) where the spectral distortions due to incident beam self-absorption or over-absorption can only be minimized but never fully excluded. Spectral distortion due to over-absorption is minimized by reducing the interaction of the incoming X-rays with the analyte until the X-ray penetration (as observed by the XES instrument) does not significantly change when the incoming energy is tuned through an absorption edge of the analyte. This is achieved either by decreasing the total absorption of the sample, i.e. making it optically thin, or by decreasing the ratio between the absorption of the analyte over the total absorption. The latter is the case when the analyte is embedded in a matrix of high Z elements.[71,72]

While it is desirable to minimize over-absorption it is not possible if the sample must be measured in its unaltered state or the particle size cannot be decreased significantly below the absorption length. The spectral distortion due to over-absorption may not critically compromise the data analysis if all spectra are measured with the same degree of distortion. One may also attempt to correct for over-absorption,[73–78] but this is not always successful as very precise knowledge of the sample (composition, homogeneity, morphology, …) may be necessary.

Alternatively, one may include over-absorption in the data analysis in order to reduce the error. An approximate equation for the fluorescence signal is[60,71]:

$$f_{OA}(x) = kx\frac{1 - e^{-\beta\,(x+\alpha)}}{x + \alpha}$$

$$x \propto \mu(E);\ \alpha = \mu_{else}(E) + g\mu_{tot}(E_f);\ \beta = \frac{d}{sin\theta};\, g = \frac{sin\theta}{sin\varphi}$$

with the analyte absorption coefficient $\mu(E)$, the sample and matrix absorption μ_{tot} and μ_{else} and the angles between incoming and outgoing beam and the sample surface θ and ϕ. The factor k lumps together subtended solid angle, fluorescence yield, incoming photon flux, and spectrometer detection efficiency. Also, the high energy resolution of XES selects only a part of the emission spectrum (e.g. around the maximum of the $K\alpha_1$ peak) further reducing the signal. The equation is approximate because a flat sample surface is assumed and the variation of the angle ϕ across the solid angle subtended by the crystal analyzer surfaces is neglected. A more precise treatment has been proposed by Trevorah et al.[74]

The equation for over-absorption cannot be solved for $\mu(E)$. While it is always desirable to obtain a physical quantity such as the photoelectric absorption coefficient in an experiment, we argue here that it is not always necessary and important conclusions can be drawn from distorted spectra. Instead of correcting the measured spectra for distortions due to self-absorption we propose to use the equation to fit a spectrum onto another spectrum that is distorted because of over-absorption. An example is shown in Figure 8 for Zn in Ga_2O_3.[79] Zn-Modified Ga_2O_3 catalysts are interesting systems for photocatalytic water splitting. The catalyst can be prepared by the impregnation method followed by thermal treatment where Zn may be incorporated as ZnO or $ZnGa_2O_4$. Zn loadings may vary between 2 and 70 weight % (wt%) and over-absorption effects will strongly change between the samples. We measured the two model compounds ZnO or $ZnGa_2O_4$ undiluted and tried to extract their contributions in the catalysts by fitting the HERFD-XANES spectra recorded on the $K\alpha_1$ line. A simple linear combination gives poor results because already the reference spectra are strongly distorted by over-absorption. By including over-absorption in the fit with α and β as fit parameters and the constraint that all spectra must be normalized to the spectral area, a considerably better fit is found. Including over-absorption gives a contribution of ZnO twice as large as in the simple linear fit. In this approach over-absorption is considered by deliberately distorting the spectra even more instead of trying to correct the distortion due to over-absorption. The fitting procedure determines the degree of induced distortion. This procedure can also be used to identify whether spectral changes are due to real chemical changes or different degrees of over-absorption.

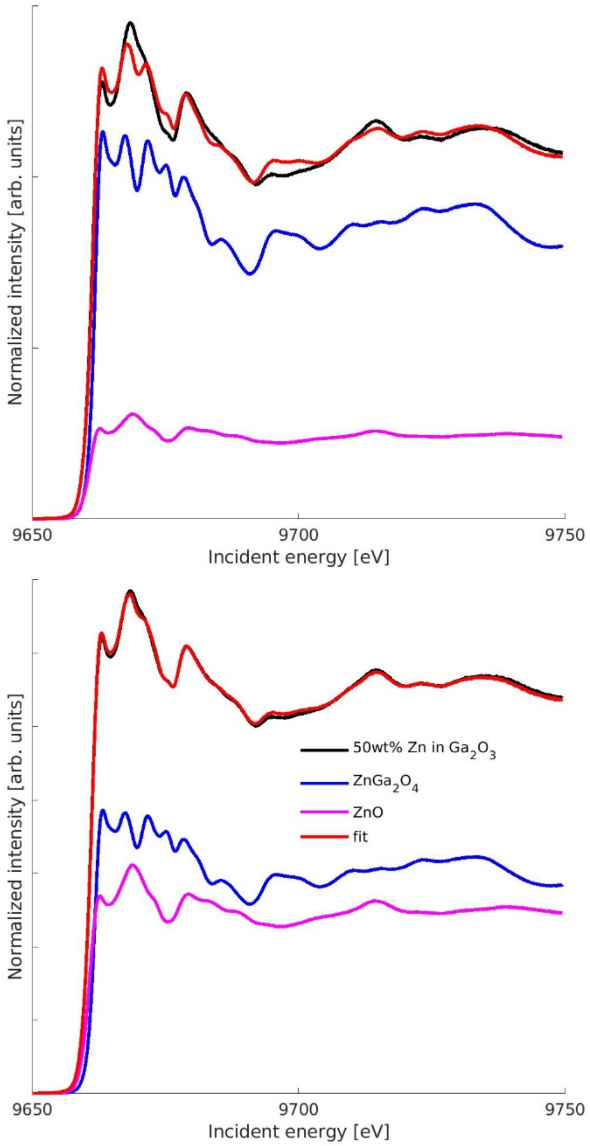

Figure 8 Kα_1-detected Zn K edge HERFD-XANES of Zn in Ga_2O_3. The spectra were recorded on undiluted samples. The spectrum with 50 wt% Zn in Ga_2O_3 was fitted without (top) and with (bottom) considering over-absorption.

Range-extended EXAFS

The extended X-ray absorption fine structure (EXAFS) signal in the XAS spectrum spans typically up to about 1 keV from the absorption edge and a sufficiently long available data range in *k* space is needed in order to perform an accurate quantitative analysis.[80] A problem often found in multi-element compounds is the unfortunate interference between the absorption edge of the element of interest and that of another element. For instance, this is the case for the W L_3 edge (10.2 keV) EXAFS signal in the perovskite oxide system $Pb_2MnW_{1-x}Re_xO_6$, where there is interference with the Re L_3 edge (10.5 keV).[81] Extending the EXAFS range beyond unwanted edges using a XES instrument has been presented previously[82–84] and it was shown that the method only works in dilute systems[60] or if the two elements are spatially separated and the unwanted element only occurs downstream of the analyte.[85] Another approach to address this problem is by combining HERFD and total fluorescence yield (TFY) simultaneous EXAFS measurements. This approach was proposed to obtain the Mn K edge (6.5 keV) EXAFS in the perovskite $Nd_{0.5}Sr_{0.5}MnO_3$, where the Nd L_2 edge (6.7 keV) overlaps in energy.[86] The unwanted absorption edge appears as a dip in the HERFD-EXAFS data because fewer incoming photons are available for the target element due to the competing absorption cross sections.[60] The contribution of the unwanted absorption edge is visible as a rise in the TFY-EXAFS data. The Mn K edge "range extended" EXAFS signal of $Nd_{0.5}Sr_{0.5}MnO_3$ can be obtained by a linear combination of the HERFD and TFY data that suppresses the contribution from the Nd L_2 edge (see Figure 9 (a)). While the contribution from the Nd L_2 edge would limit the EXAFS range in *k* space to about 7 $Å^{-1}$, the range extended EXAFS obtained in this way spans much further (see Figure 9(b)). This approach is successful because the inverted edge absorption in the HERFD-XAS data is not spectral sharpened and has thus the same spectral width as the TFY data. The potential of this approach may be especially valuable in the EXAFS characterization of multi-component nanosized systems like particles or thin films where many elements usually coexist and edge interference is thus highly probable.

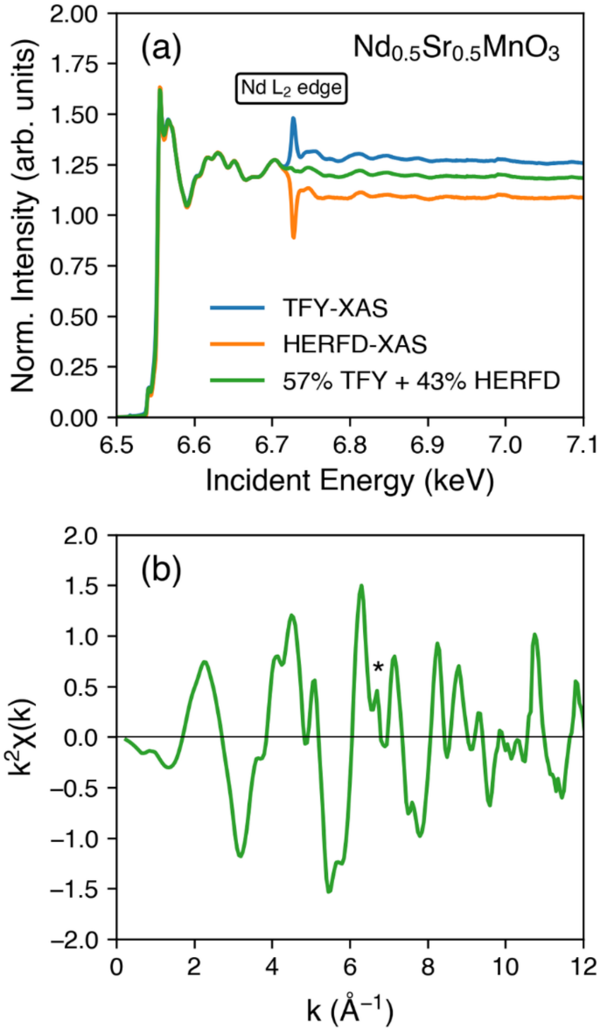

Figure 9 Range extended Mn K edge EXAFS of $Nd_{0.5}Sr_{0.5}MnO_3$ at 80 K. (a) Comparison between TFY- and HERFD-XAS data showing the Nd L_2 edge contribution and the linear combination between the two used to yield the range extended Mn K edge EXAFS. (b) $k^2\chi(k)$ signal in k space where the asterisk indicates the position corresponding to the Nd L_2 edge energy.

The choice of emission energy in HERFD-XANES

HERFD-XANES is RIXS and the spectral shape thus depends on the incoming and outgoing (emission) energy. In many HERFD-XANES studies it is not possible to record a full RIXS plane (because of e.g. radiation damage, low analyte concentration, time evolution). The emission lines are chemically sensitive, i.e. the emission peak maximum may change with the analyte chemical state, and the question arises whether or not to change the emission energy for recording HERFD-XAS when the sample undergoes a transition or for comparison between different samples. One may choose to always tune the XES instrument to the maximum of the emission line. This requires a scan of the emission energy to determine the maximum before each HERFD-XAS scan. Alternatively, one chooses to use the same emission energy for the entire study. In this case, it is important to carefully assess the chemical sensitivity of the emission lines using model compounds and study its effect on the HERFD-XANES data. Figure 10 shows as example a series of Ce L_3 edge HERFD-XANES spectra of CeO_2 at different emission energies around the $L\alpha_1$ emission line maximum.[30,87] Different emission energies yield different edge positions and HERFD-XANES spectral shapes. The best experimental strategy to adopt depends on the study at hand. The problem is most pertinent when the emission lines show a strong chemical sensitivity, *e.g.* the $K\beta$ lines in 3*d* transition metals. The deeper the core hole in the final state, the weaker the chemical dependence, e.g. the $L\alpha$ lines of 5*d* transition metals where additionally the large core hole lifetime broadening masks the chemical shift.

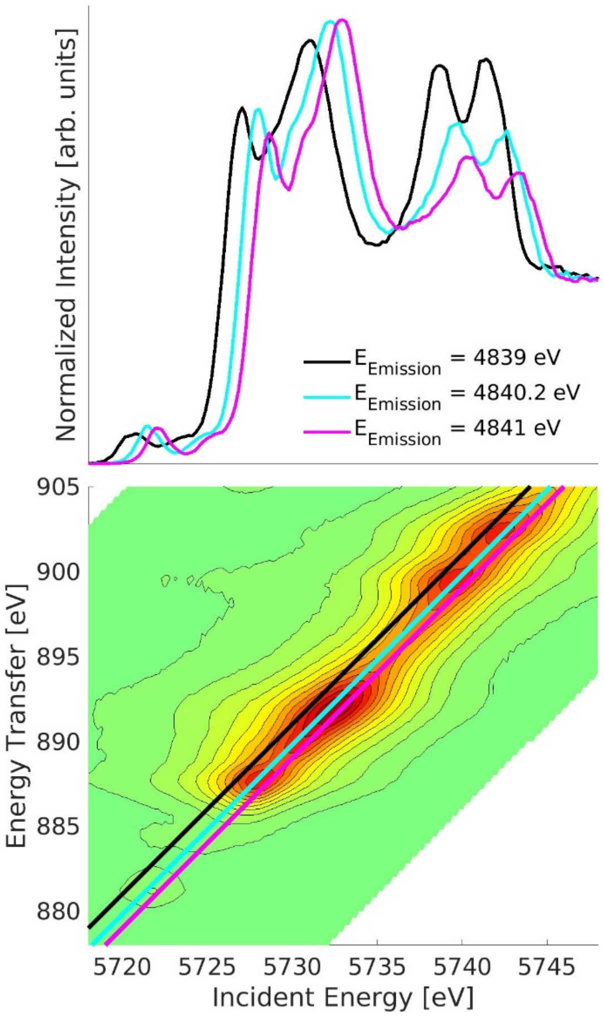

Figure 10 Ce L_3 edge HERFD-XANES of CeO_2 detected at different emission energies (top). Diagonal cuts in the energy transfer versus incident energy RIXS map indicate the selected emission energies around the $L\alpha_1$ emission line (bottom). By varying the emission energy, the HERFD-XANES spectra shift in energy and change shape.

Colloidal nanoparticles

The term colloidal nanoparticles (NPs) refers to a mixture of solid nanosized particles (below 100 nm in at least one dimension) and a liquid medium such that Brownian agitation overcomes any settling motion due to gravity.[88] Among them, colloidal magnetic NPs, which consist of materials that are ferro- or ferrimagnetic in its bulk form, are currently intensively investigated as they lead to many important applications spanning from biomedicine to mechanical engineering.[89] However, despite the impressive progress in the different chemical routes to obtain colloidal magnetic NPs with controlled dimensions, shape, crystallinity, size distribution, surface chemistry, or even hybrid structures, the resultant physico-chemical properties and their precise relationship with all these characteristics are still not well understood. Within this context, PIPO spectroscopies appear as valuable tools to obtain chemical, structural, electronic, and magnetic information with element-selectivity. Hard X-ray PIPO spectroscopic techniques are ideal for investigating colloidal NPs under *in situ* conditions (that is, directly in the carrier liquid) due to two main reasons. First, PIPO spectroscopies such as HERFD-XAS or RIXS, may provide considerably more information on the electronic structure than standard (photon-in) XAS. In addition to the spectral sharpening effect described before, the two-dimensional character of PIPO may also lead to extra features like magnetic moment information with site-selectivity in the combination of RIXS and XMCD, RIXS-MCD.[90,91] Secondly, the use of hard X-rays implies both bulk sensitivity and compatibility with complex sample environments since ultra-high vacuum conditions are not required. The probing depth is about a few µm versus a few nm for soft X-rays when using total electron yield, which ensures that the whole volume, and not only the outermost part, is probed. The bulk sensitivity has been recently exploited in the RIXS-MCD characterization of various nanosized materials where it was needed to access the entire volume: from buried thin films of a few tens of nm[92] to bimagnetic core-shell NPs in powder[93] and liquid phase[94] or even binary ferrofluids composed of two magnetically different types of NPs.[95] The magneto-spectroscopy RIXS-MCD is indeed very well suited for investigating magnetic colloidal NPs in the liquid phase. The *in situ* characterization is an important aspect as the physico-chemical properties of the NPs may change in the powder form. For instance, in powder the NPs agglomerate considerably more than in suspension. The properties of the NPs can also be altered under the vacuum conditions required by soft X-rays and measurements of the NPs directly in dispersion in this energy regime are experimentally rather challenging.[96] In the following, we provide two examples on the applicability of bulk-sensitive site-selective RIXS-MCD (and HERFD-XANES implicitly) for characterization of magnetic NPs in colloidal solution.

The first example deals with magnetite Fe_3O_4 nanoparticles measured in a liquid jet setup. These iron oxide NPs are one of the most investigated magnetic systems mainly due to their biocompatibility and hence the potential for biomedical applications.[97–101] These applications stem from the superparamagnetic behaviour exhibited by sufficiently small Fe_3O_4 NPs at room temperature, while at cryogenic temperatures they are typically ferromagnetic. An interesting experimental method for RIXS-MCD *in situ* characterization of magnetic colloidal NPs at room temperature is the use of a liquid jet setup available at ID26 beamline of the ESRF (see Figure 11(a)). It is based on the same concept of a setup previously used for HERFD-XAS measurements in CeO_2 colloidal NPs[30] but in this case a pump compatible with magnetic solutions and a magnet required for RIXS-MCD are included. The sample is in a reservoir under magnetic stirring to ensure homogeneity. By means of a rotatory gear pump a continuous flow is produced that forms a freestanding jet after passing through a 1 mm open capillary and finally goes back to the reservoir. The incident X-rays shine on the freestanding jet and a compact electromagnet (field up to ±0.5 Tesla) is incorporated to provide magnetic saturation in the same sample spot illuminated by the X-rays.

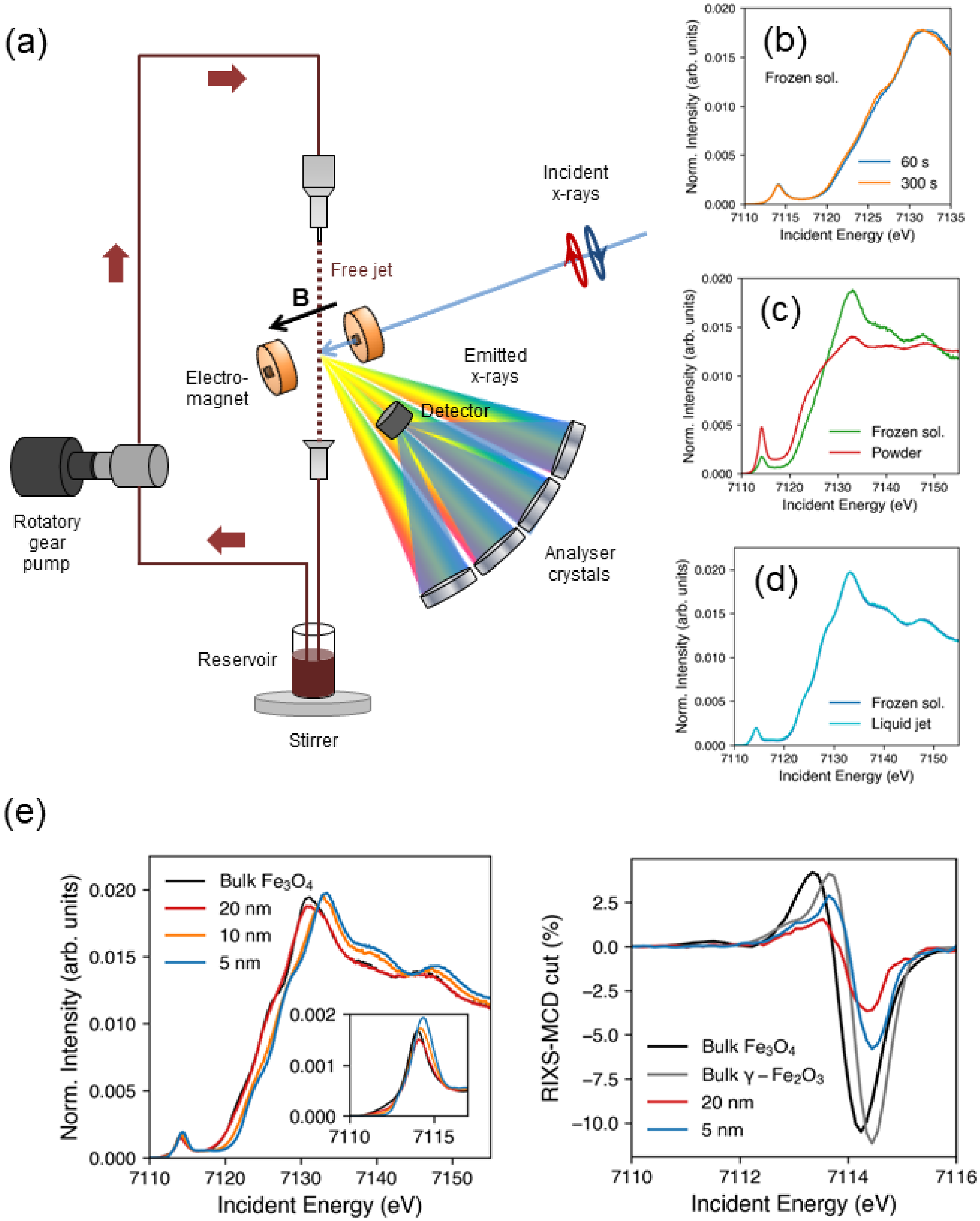

Figure 11 $K\alpha_1$-detected Fe K edge HERFD-XANES and 1s2p RIXS-MCD data of Fe_3O_4 NPs measured in a liquid jet setup. (a) Scheme of the continuous flow liquid jet setup for RIXS-MCD experiments at beamline ID26 of the ESRF. (b) HERFD-XANES spectra of 7 nm Fe_3O_4 NPs measured as frozen solution at different total illumination times. (c) HERFD-XANES spectra of 15 nm Fe_3O_4 NPs measured in frozen solution and powder forms. (d) HERFD-XANES spectra of 5 nm Fe_3O_4 NPs measured as frozen solution and in the liquid jet setup. (e) HERFD-XANES spectra and RIXS-MCD cuts of a set of commercial Fe_3O_4 spherical NPs (20, 10, and 5 nm size) measured in the liquid jet compared with bulk references.

In order to assess the potential of this experimental method, Fe K edge HERFD-XANES spectra measured in the liquid jet were compared with data collected in a He-flow cryostat in frozen solution and powder forms. Measurements in frozen solutions revealed photoreduction effects especially in small NPs (see Figure 11b) and thus impose a limitation on the total illumination time per sample spot. In addition to this, in powder form the distortion in the spectral shape due to self-absorption is much more likely to limit the data collection due to particle agglomeration (see Figure 11(c)). In the liquid jet setup, the sample is continuously circulating, and the incident X-rays always shine on a fresh spot given the large sample volume (around a few tens of ml), which is very useful to exclude radiation damage effects that complicate measurements in static samples. This is particularly relevant for highly time-consuming measurements as RIXS-MCD. Upon careful radiation damage evaluation in frozen solution form samples, a very good consistency is found with liquid jet measurements (see Figure 11(d)). We note that measurements in the frozen solution do not reproduce the conditions for the biomedical applications and the characterization of the sample at room temperature may be preferred.

A set of commercially available Fe_3O_4 spherical NPs in solution (20, 10, and 5 nm) was characterized by HERFD-XANES and RIXS-MCD measurements in the liquid jet setup (Figure 11(e)). The samples were supplied by Sigma-Aldrich and they were dispersed in toluene. The HERFD-XANES spectra reveal significant size-dependent changes in both the main edge and pre-edge region. The edge energy position of the 20 nm sample reasonably agrees with bulk Fe_3O_4, but a chemical shift towards a more oxidized phase is observed when decreasing the size to 10 and 5 nm. 1*s*2*p* RIXS-MCD data were measured in the 20 nm and 5 nm samples at the maximum of the Fe $K\alpha_1$ line, which corresponds to a diagonal cut in the two-dimensional RIXS-MCD map.[90,91] Compared with bulk Fe_3O_4 and maghemite γ-Fe_2O_3 (Fe^{2+}-deficient form of magnetite), both samples show a considerably reduced amplitude in the dichroic difference signal. The main contribution to the RIXS-MCD signal in magnetite and maghemite comes from the Fe^{3+} tetrahedral (T_d) site.[90,93] The small RIXS-MCD amplitude compared with the bulk oxides indicates that the magnetic properties of the NPs are strongly affected by the size reduction with a lower long range ordered magnetic moment in the Fe^{3+} T_d site sublattice for the 20 nm NPs than for the 5 nm. Finally, from a technical viewpoint, these RIXS-MCD results measured in a liquid jet setup show the feasibility of the method and open up the door for bulk-sensitive magneto-spectroscopic characterization of ferrofluids without the need to freeze the sample and avoiding possible radiation damage.

Note added. A new experimental approach for RIXS-MCD characterization of magnetic colloidal NPs in the liquid phase at room temperature inside a capillary is presented in the communication by J. Kuciakowski et al. in the same special issue (Manuscript ID NR-COM-04-2020-002866, currently under minor revision).

The second example of application of RIXS-MCD on magnetic NPs in the liquid phase is given by the study of 7 nm core-shell $MnFe_2O_4$@$CoFe_2O_4$ NPs performed by N. Daffé and co-workers.[94] The magnetic properties of spinel ferrite colloidal NPs can be tuned further by combining deliberately two different phases in a core-shell structure. The idea is to modulate the magnetic anisotropy to enhance the performance in selected applications. The bimagnetic NPs investigated by N. Daffé and co-workers consist of a core of magnetically soft $MnFe_2O_4$ and a shell of magnetically hard $CoFe_2O_4$ with a very thin thickness (0.5 nm). 1*s*2*p* RIXS-MCD was applied at the K pre-edge of both Mn and Co to study the two magnetic phases. The measurements were performed on the frozen phase of the samples (below the freezing temperature of the carrier liquid, heptane) in a He-flow cryostat using a dedicated cryo-liquid cell.[95] They were kept in magnetic saturation using an electromagnet that provided a field up to ±1.5 Tesla. A strong dichroic signal ascribed to the contribution of tetrahedral Mn^{2+} ions was found in the Mn RIXS-MCD map (see Figure 10(a)), while a weak signal with opposite sign was obtained in the Co RIXS-MCD map (see Figure 10(b)) in agreement with the presence of octahedral Co^{2+} ions. This result demonstrates the ferromagnetic coupling between the core and the shell. In addition, the authors investigated the soft/hard magnetic character of the core and shell components by performing site-selective hysteresis loops sweeping the magnetic field (B) at maximum intensity RIXS-MCD features (i.e., at constant incident and emission energies). These results were compared with similar loops obtained using soft X-ray standard (photon-in) XMCD, with a probing depth of only 2 nm. For the $MnFe_2O_4$ core (see Figure 10(c)), the RIXS-MCD loop displays very large values of coercivity indicating an unexpected hard magnet character since $MnFe_2O_4$ is a typical soft material. In the case of the CoFe2O4 shell (0.5 nm thick), the same hard magnet behaviour was obtained in both experiments (see Figure 10(c)). Meanwhile, the soft X-ray XMCD loop of the $MnFe_2O_4$ core, only sensitive to the outermost layers, shows a coercivity comparable to that of the Co ions in the shell. It was then concluded that a strong magnetic anisotropy is imposed from the shell to the core, from low coercivity at the core-shell interface to large coercivity inside the core. This unusual magnetic behaviour in core-shell $MnFe_2O_4$@$CoFe_2O_4$ NPs could only be accessed by the combination of site-selective and bulk-sensitive RIXS-MCD with surface-sensitive XMCD.

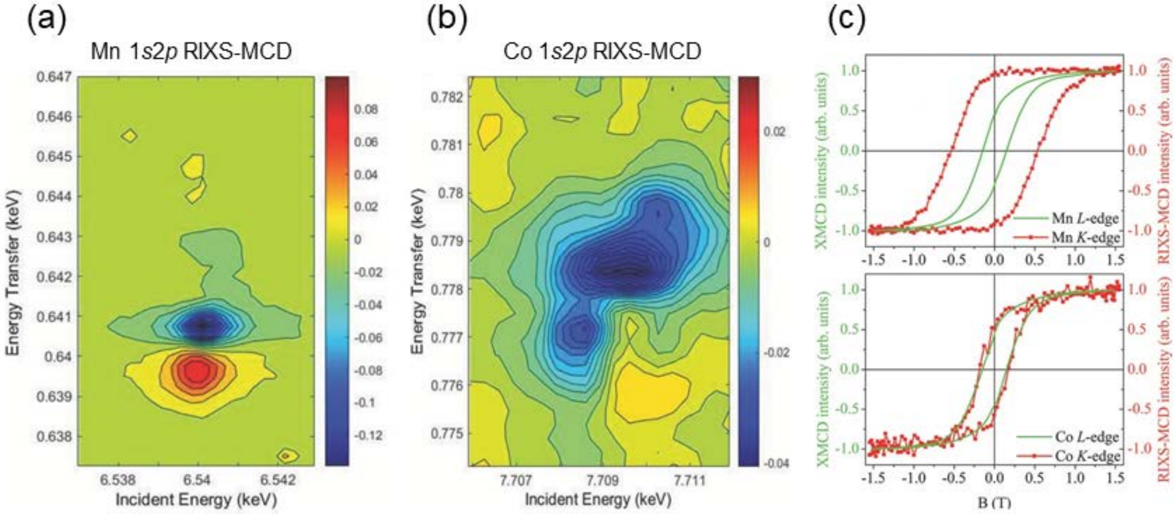

Figure 12 1s2p RIXS-MCD data of core-shell $MnFe_2O_4$@$CoFe_2O_4$ 7 nm NPs measured as frozen solution in a dedicated liquid cell. RIXS-MCD maps measured at the (a) Mn and (b) Co K pre-edge region. (c) Hysteresis loops for Mn and Co obtained at the maximum of the dichroic signal in soft X-ray XMCD (L edge) and in RIXS-MCD (K edge). Adapted with permission from N. Daffé et al.[94] *Copyright © 2017, John Wiley and Sons.*

Conclusions

An X-ray emission spectrometer adds a spectroscopic dimension to X-ray absorption spectroscopy. Photon-in/photon-out spectroscopy dramatically advances the element-selective study of electronic structure and coordination. The technique brings new possibilities that require careful study and understanding. Radiation damage is an important challenge for high brilliance beamlines and must take high priority for all experimental sessions. The instrumentation can be further improved in particular with respect to the captured solid angle. We think that the possibilities of PIPO are still not fully explored and we hope that this paper contributes to the understanding and improving of the experimental possibilities and triggers ideas for future studies.

Acknowledgements

The authors would like to thank T. Bohdan, M. Rovezzi, P. van der Linden, and Y. Watier for their help with the liquid jet setup for RIXS-MCD. We also thank H. Elnaggar, M. Busquets-Fité, J. Cruces-Muro, A. G. Roca, and J. Piella for collaborating on the measurements of Fe_3O_4 nanoparticles.

References

1 P. Glatzel and U. Bergmann, *Coord. Chem. Rev.*, 2005, 249, 65–95.

2 P. Glatzel, T. C. Weng, K. Kvashnina, J. Swarbrick, M. Sikora, E. Gallo, N. Smolentsev and R. A. Mori, *J. Electron Spectros. Relat. Phenomena*, 2013, **188**, 17–25.

3 A. Kalinko, W. A. Caliebe, R. Schoch and M. Bauer, *J. Synchrotron Radiat.*, 2020, **27**, 31–36.

4 K. Klementiev, I. Preda, S. Carlson, K. Sigfridsson and K. Norén, *J. Phys. Conf. Ser*, 2016, **712**, 12018.

5 M. Moretti Sala, K. Martel, C. Henriquet, A. Al Zein, L. Simonelli, C. J. Sahle, H. Gonzalez, M.-C. Lagier, C. Ponchut, S. Huotari, R. Verbeni, M. Krisch and G. Monaco, *J. Synchrotron Radiat.*, 2018, **25**, 580–591.

6 M. Rovezzi, C. Lapras, A. Manceau, P. Glatzel and R. Verbeni, *Rev. Sci. Instrum.*, 2017, **88**, 013108.

7 J. L. Hazemann, O. Proux, V. Nassif, H. Palancher, E. Lahera, C. Da Silva, A. Braillard, D. Testemale, M. A. Diot, I. Alliot, W. Del Net, A. Manceau, F. Gélébart, M. Morand, Q. Dermigny and A. Shukla, *J. Synchrotron Radiat.*, 2009, **16**, 283–292.

8 I. Llorens, E. Lahera, W. Delnet, O. Proux, A. Braillard, J.-L. L. Hazemann, A. Prat, D. Testemale, Q. Dermigny, F. Gelebart, M. Morand, A. Shukla, N. Bardou, O. Ulrich, S. Arnaud, J.-F. F. Berar, N. Boudet, B. Caillot, P. Chaurand, J. Rose, E. Doelsch, P. Martin and P. L. Solari, *Rev. Sci. Instrum.*, 2012, **83**, 063104.

9 K. O. Kvashnina and A. C. Scheinost, *J. Synchrotron Radiat.*, 2016, **23**, 836–841.

10 B. Mei, S. Gu, X. Du, Z. Li, H. Cao, F. Song, Y. Huang and Z. Jiang, *X-Ray Spectrom.*, 2020, **49**, 251–259.

11 J. M. Ablett, D. Prieur, D. Céolin, B. Lassalle-Kaiser, B. Lebert, M. Sauvage, T. Moreno, S. Bac, V. Balédent, A. Ovono, M. Morand, F. Gélebart, A. Shukla and J. P. Rueff, *J. Synchrotron Radiat.*, 2019, **26**, 263–271.

12 E. Kleymenov, J. A. van Bokhoven, C. David, P. Glatzel, M. Janousch, R. Alonso-Mori, M. Studer, M. Willimann, A. Bergamaschi, B. Henrich and M. Nachtegaal, *Rev. Sci. Instrum.*, 2011, **82**, 065107.

13 J. Szlachetko, M. Nachtegaal, E. De Boni, M. Willimann, O. Safonova, J. Sa, G. Smolentsev, M. Szlachetko, J. A. Van Bokhoven, J. C. Dousse, J. Hoszowska, Y. Kayser, P. Jagodzinski, A. Bergamaschi, B. Schmitt, C. David and A. Lücke, *Rev. Sci. Instrum.*, 2012, **83**, 103105.

14 R. Alonso-Mori, J. Kern, D. Sokaras, T. C. Weng, D. Nordlund, R. Tran, P. Montanez, J. Delor, V. K. Yachandra, J. Yano and U. Bergmann, *Rev. Sci. Instrum.*, 2012, **83**, 073114.

15 D. Sokaras, T. C. Weng, D. Nordlund, R. Alonso-Mori, P. Velikov, D. Wenger, A. Garachtchenko, M. George, V. Borzenets, B. Johnson, T. Rabedeau and U. Bergmann, *Rev. Sci. Instrum.*, 2013, **84**, 053102.

16 S. H. Nowak, R. Armenta, C. P. Schwartz, A. Gallo, B. Abraham, A. T. Garcia-Esparza, E. Biasin, A. Prado, A. Maciel, D. Zhang, D. Day, S. Christensen, T. Kroll, R. Alonso-Mori, D. Nordlund, T. C. Weng and D. Sokaras, *Rev. Sci. Instrum.*, 2020, **91**, 033101.

17 M. Rovezzi, A. Harris, B. Detlefs, T. Bohdan, A. Svyazhin, A. Santambrogio, D. Degler, R. Baran, B. Reynier, P. Noguera Crespo, C. Heyman, H. P. Van Der Kleij, P. Van Vaerenbergh, P. Marion, H. Vitoux, C. Lapras, R. Verbeni, M. M. Kocsis, A. Manceau and P. Glatzel, *J. Synchrotron Radiat.*, 2020, **27**, 813–826.

18 U. Zastrau, L. B. Fletcher, E. Förster, E. C. Galtier, E. Gamboa, S. H. Glenzer, P. Heimann, H. Marschner, B. Nagler, A. Schropp, O. Wehrhan and H. J. Lee, *Rev. Sci. Instrum.*, 2014, **85**, 093106.

19 E. P. Jahrman, W. M. Holden, A. S. Ditter, D. R. Mortensen, G. T. Seidler, T. T. Fister, S. A. Kozimor, L. F. J. Piper, J. Rana, N. C. Hyatt and M. C. Stennett, *Rev. Sci. Instrum.*, 2019, **90**, 024106.

20 G. T. Seidler, D. R. Mortensen, A. J. Remesnik, J. I. Pacold, N. A. Ball, N. Barry, M. Styczinski and O. R. Hoidn, *Rev. Sci. Instrum.*, 2014, **85**, 113906.

21 A. P. Honkanen, S. Ollikkala, T. Ahopelto, A. J. Kallio, M. Blomberg and S. Huotari, *Rev. Sci. Instrum.*, 2019, **90**, 033107.

22 W. Malzer, D. Grötzsch, R. Gnewkow, C. Schlesiger, F. Kowalewski, B. Van Kuiken, S. Debeer and B. Kanngießer, *Rev. Sci. Instrum.*, 2018, **89**, 1–8.

23 Z. Németh, J. Szlachetko, É. G. Bajnóczi and G. Vankó, *Rev. Sci. Instrum.*, 2016, **87**, 103105.

24 L. Anklamm, C. Schlesiger, W. Malzer, D. Grötzsch, M. Neitzel and B. Kanngießer, *Rev. Sci. Instrum.*, 2014, **85**, 053110.

25 W. B. Doriese, P. Abbamonte, B. K. Alpert, D. A. Bennett, E. V. Denison, Y. Fang, D. A. Fischer, C. P. Fitzgerald, J. W. Fowler, J. D. Gard, J. P. Hays-Wehle, G. C. Hilton, C. Jaye, J. L. McChesney, L. Miaja-Avila, K. M. Morgan, Y. I. Joe, G. C. O'Neil, C. D. Reintsema, F. Rodolakis, D. R. Schmidt, H. Tatsuno, J. Uhlig, L. R. Vale, J. N. Ullom and D. S. Swetz, *Rev. Sci. Instrum.*, 2017, **88**, 053108.

26 N. B. Brookes, F. Yakhou-Harris, K. Kummer, A. Fondacaro, J. C. Cezar, D. Betto, E. Velez-Fort, A. Amorese, G. Ghiringhelli, L. Braicovich, R. Barrett, G. Berruyer, F. Cianciosi, L. Eybert, P. Marion, P. van der Linden and L. Zhang, *Nucl. Instrum. Methods Phys. Res., Sect. A*, 2018, **903**, 175–192.

27 A. Manceau, M. Enescu, A. Simionovici, M. Lanson, M. Gonzalez-Rey, M. Rovezzi, R. Tucoulou, P. Glatzel, K. L. Nagy and J.-P. Bourdineaud, *Environ. Sci. Technol.*, 2016, **50**, 10721–10729.

28 M. Merkulova, O. Mathon, P. Glatzel, M. Rovezzi, V. Batanova, P. Marion, M.-C. Boiron and A. Manceau, *ACS Earth Space Chem.*, 2019, **3**, 1905–1914.

29 R. G. Castillo, R. Banerjee, C. J. Allpress, G. T. Rohde, E. Bill, L. Que, J. D. Lipscomb and S. DeBeer, *J. Am. Chem. Soc.*, 2017, **139**, 18024–18033.

30 J. D. Cafun, K. O. Kvashnina, E. Casals, V. F. Puntes and P. Glatzel, *ACS Nano*, 2013, **7**, 10726–10732.

31 E. F. Garman and M. Weik, in *Protein Crystallography: Challenges and Practical Solutions*, ed. K. Beis and G. Evans, Royal Society of Chemistry, London, 2018, ch. 4, pp. 88-116.

32 J. Wang, G. A. Botton, M. M. West and A. P. Hitchcock, *J. Phys. Chem. B*, 2009, **113**, 1869–1876.

33 S. Della Longa and A. Arcovito, *Inorg. Chem.*, 2010, **49**, 9958–9961.

34 H. Yamane, M. Oura, K. Sawada, T. Ebisu, T. Ishikawa, N. Yamazaki, K. Hasegawa, K. Takagi and T. Hatsui, *J. Electron Spectros. Relat. Phenomena*, 2019, **232**, 11–15.

35 C. G. Frankaer, S. Mossin, K. Ståhl and P. Harris, *Acta Crystallogr. Sect. D Biol. Crystallogr.*, 2014, **70**, 110–122.

36 C. Gervais, M. Thoury, S. Réguer, P. Gueriau and J. Mass, *Appl. Phys. A Mater. Sci. Process.*, 2015, **121**, 949–955.

37 E. De La Mora, J. E. Lovett, C. F. Blanford, E. F. Garman, B. Valderrama and E. Rudino-Pinera, *Acta Crystallogr. Sect. D Biol. Crystallogr.*, 2012, **68**, 564–577.

38 A. Adriaens, P. Quinn, S. Nikitenko and M. G. Dowsett, *Anal. Chem.*, 2013, **85**, 9556–9563.

39 M. M. Van Schooneveld and S. DeBeer, *J. Electron Spectros. Relat. Phenomena*, 2015, **198**, 31–56.

40 J. Yano, J. Kern, K.-D. Irrgang, M. J. Latimer, U. Bergmann, P. Glatzel, Y. Pushkar, J. Biesiadka, B. Loll, K. Sauer, J. Messinger, A. Zouni and V. K. Yachandra, *Proc. Natl. Acad. Sci. U. S. A.*, 2005, **102**, 12047–52.

41 F. Porcaro, S. Roudeau, A. Carmona and R. Ortega, *TrAC - Trends Anal. Chem.*, 2018, **104**, 22–41.

42 S. Y. Chang, A. Uehara, S. G. Booth, K. Ignatyev, J. F. W. Mosselmans, R. A. W. Dryfe and S. L. M. Schroeder, *RSC Adv.*, 2015, **5**, 6912–6918.

43 V. Vercamer, PhD Thesis, Université Pierre et Marie Curie - Paris VI, 2016.

44 M. Kubin, J. Kern, M. Guo, E. Källman, R. Mitzner, V. K. Yachandra, M. Lundberg, J. Yano and P. Wernet, *Phys. Chem. Chem. Phys.*, 2018, **20**, 16817–16827.

45 Z. W. Lebens-Higgins, J. Vinckeviciute, J. Wu, N. V. Faenza, Y. Li, S. Sallis, N. Pereira, Y. S. Meng, G. G. Amatucci, A. Van Der Ven, W. Yang and L. F. J. Piper, *J. Phys. Chem. C*, 2019, **123**, 13201–13207.

46 J. M. Ramallo-López, L. J. Giovanetti, F. C. Vicentin and F. G. Requejo, *J. Phys. Conf. Ser.*, 2013, **430**, 012034.

47 M. N. Revoy, R. W. J. Scott and A. P. Grosvenor, *J. Phys. Chem. C*, 2013, **117**, 10095–10105.

48 R. Terzano, T. Mimmo, B. Vekemans, L. Vincze, G. Falkenberg, N. Tomasi, M. Schnell Ramos, R. Pinton and S. Cesco, *Anal. Bioanal. Chem.*, 2013, **405**, 5411–5419.

49 P. Glatzel, R. Alonso-mori and D. Sokaras, in *X-Ray Absorption and X-Ray Emission Spectroscopy: Theory and Applications*, ed. J. A. van Bokhoven and C. Lamberti, John Wiley & Sons, Ltd, Chichester, 2016, ch. 6, pp. 125–153.

50 R. Alonso-Mori, J. Kern, R. J. Gildea, D. Sokaras, T. C. Weng, B. Lassalle-Kaiser, R. Tran, J. Hattne, H. Laksmono, J. Hellmich, C. Glöckner, N. Echols, R. G. Sierra, D. W. Schafer, J. Sellberg, C. Kenney,

R. Herbst, J. Pines, P. Hart, S. Herrmann, R. W. Grosse-Kunstleve, M. J. Latimer, A. R. Fry, M. M. Messerschmidt, A. Miahnahri, M. M. Seibert, P. H. Zwart, W. E. White, P. D. Adams, M. J. Bogan, S. Boutet, G. J. Williams, A. Zouni, J. Messinger, P. Glatzel, N. K. Sauter, V. K. Yachandra, J. Yano, U. Bergmann, C. Glockner, N. Echols, R. G. Sierra, D. W. Schafer, J. Sellberg, C. Kenney, R. Herbst, J. Pines, P. Hart, S. Herrmann, R. W. Grosse-Kunstleve, M. J. Latimer, A. R. Fry, M. M. Messerschmidt, A. Miahnahri, M. M. Seibert, P. H. Zwart, W. E. White, P. D. Adams, M. J. Bogan, S. Boutet, G. J. Williams, A. Zouni, J. Messinger, P. Glatzel, N. K. Sauter, V. K. Yachandra, J. Yano and U. Bergmann, *Proc. Natl. Acad. Sci. U. S. A.*, 2012, **109**, 19103–19107.

51 E. Gallo and P. Glatzel, *Adv. Mater.*, 2014, **26**, 7730–7746.

52 R. G. Castillo, J. T. Henthorn, J. McGale, D. Maganas and S. DeBeer, *Angew. Chem.*, Int. Ed., 2020, **59**, 2-13

53 C. J. Pollock and S. DeBeer, *Acc. Chem. Res.*, 2015, **48**, 2967–2975.

54 J. Baumgartner, N. Menguy, T. P. Gonzalez, G. Morin, M. Widdrat and D. Faivre, *J. R. Soc. Interface*, 2016, **13**, 20160665.

55 M. Benfatto, J. A. Solera, J. García Ruiz and J. Chaboy, *Chem. Phys.*, 2002, **282**, 441–450.

56 J. García, G. Subías, V. Cuartero and J. Herrero-Martin, J. Synchrotron Radiat., 2010, **17**, 386–392.

57 P. Wang, B. A. McKenna, N. W. Menzies, C. Li, C. J. Glover, F. J. Zhao and P. M. Kopittke, *J. Synchrotron Radiat.*, 2019, **26**, 1272–1279.

58 P. Glatzel, U. Bergmann, F. M. F. De Groot and S. P. Cramer, *AIP Conf. Proc.*, 2003, **652**, 250.

59 Y. Pushkar, X. Long, P. Glatzel, G. W. Brudvig, G. C. Dismukes, T. J. Collins, V. K. Yachandra, J. Yano and U. Bergmann, *Angew. Chem., Int. Ed.*, 2010, **49**, 800–803.

60 M. Bianchini and P. Glatzel, *J. Synchrotron Radiat.*, 2012, **19**, 911–919.

61 J. Yano and V. Yachandra, *Chem. Rev.*, 2014, **114**, 4175–4205.

62 V. Krewald, M. Retegan, N. Cox, J. Messinger, W. Lubitz, S. DeBeer, F. Neese and D. A. Pantazis, *Chem. Sci.*, 2015, **6**, 1676–1695.

63 M. A. Beckwith, M. Roemelt, M. N. Collomb, C. Duboc, T. C. Weng, U. Bergmann, P. Glatzel, F. Neese and S. Debeer, *Inorg. Chem.*, 2011, **50**, 8397–8409.

64 P. Glatzel, H. Schroeder, Y. Pushkar, T. Boron, S. Mukherjee, G. Christou, V. L. Pecoraro, J. Messinger, V. K. Yachandra, U. Bergmann and J. Yano, *Inorg. Chem.*, 2013, **52**, 5642–5644.

65 J. Messinger, J. H. Robblee, U. Bergmann, C. Fernandez, P. Glatzel, H. Visser, R. M. Cinco, K. L. McFarlane, E. Bellacchio, S. A. Pizarro, S. P. Cramer, K. Sauer, M. P. Klein and V. K. Yachandra, *J. Am. Chem. Soc.*, 2001, **123**, 7804-7820.

66 L. Mino, V. Bonino, F. Picollo, M. Fretto, A. Agostino and M. Truccato, *Adv. Electron. Mater.*, 2019, **5**, 1900129.

67 G. Vankó, F. Renz, G. Molnár, T. Neisius and S. Kárpáti, *Angew. Chem., Int. Ed.*, 2007, **46**, 5306–5309.

68 L. Amidani, K. Korthout, J. J. Joos, M. van der Linden, H. F. Sijbom, A. Meijerink, D. Poelman, P. F.

Smet and P. Glatzel, *Chem. Mater.*, 2017, **29**, 10122–10129.

69 K. Hämäläinen, D. P. Siddons, J. B. Hastings and L. E. Berman, *Phys. Rev. Lett.*, 1991, **67**, 2850–2853.

70 P. Carra, M. Fabrizio and B. T. Thole, *Phys. Rev. Lett.*, 1995, **74**, 3700–3703.

71 Grant Bunker, *Introduction to XAFS: A Practical Guide to X-ray Absorption Fine Structure Spectroscopy*, Cambridge University Press, Cambridge, 2010.

72 S. Calvin, *XAFS for everyone*, CRC Press, Boca Raton, 2013

73 D. Haskel, FLUO: Correcting XANES for self absorption in fluorescence data, https://www3.aps.anl.gov/haskel/fluo.html.

74 R. M. Trevorah, C. T. Chantler and M. J. Schalken, *IUCrJ*, 2019, **6**, 586–602.

75 L. Troger, D. Arvantits, K. Aberschke, H. Michaelis, U. Grimm and E. Zschech, *Phys. Rev. B*, 1992, **46**, 3283–3289.

76 P. Pfalzer, J.-P. Urbach, M. Klemm, S. Horn, M. L. DenBoer, A. I. Frenkel and J. P. Kirkland, *Phys. Rev. B*, 1999, **60**, 9335–9339.

77 K. V. Klementiev, XANES dactyloscope.

78 A. Manceau, M. A. Marcus and N. Tamura, *Rev. Mineral. Geochem.*, 2002, **49**, 341-428.

79 M. Borges Ordoño, S. Yasumura, P. Glatzel and A. Urakawa, *Phys. Chem. Chem. Phys.*, 2018, **20**, 23515–23521.

80 D. C. Koningsberger, B. L. Mojet, G. E. Van Dorssen and D. E. Ramaker, *Top. Catal.*, 2000, **10**, 143–155.

81 S. Lafuerza, J. Blasco, J. García, G. Subías, V. Cuartero and R. I. Merino, *J. Phys. Condens. Matter,* 2012, **24**, 075403.

82 P. Glatzel, F. M. F. De Groot, O. Manoilova, D. Grandjean, B. M. M. Weckhuysen, U. Bergmann and R. Barrea, *Phys. Rev. B: Condens. Matter Mater. Phys.*, 2005, **72**, 14117.

83 J. Yano, Y. Pushkar, P. Glatzel, A. Lewis, K. Sauer, J. Messinger, U. Bergmann and V. Yachandra, *J. Am. Chem. Soc.*, 2005, **127**, 14974–14975.

84 H. Asakura, N. Kawamura, M. Mizumaki, K. Nitta, K. Ishii, S. Hosokawa, K. Teramura and T. Tanaka, *J. Anal. At. Spectrom.*, 2018, **33**, 84 - 89.

85 M. Hübner, D. Koziej, M. Bauer, N. Barsan, K. Kvashnina, M. D. Rossell, U. Weimar and J.-D. Grunwaldt, *Angew. Chemie, Int. Ed.*, 2011, **50**, 2841–2844.

86 S. Lafuerza, J. Garcia, G. Subias, J. Blasco and P. Glatzel, *Phys. Rev. B: Condens. Matter Mater. Phys.*, 2016, **93**, 205108.

87 A. Kotani, K. O. Kvashnina, S. M. Butorin and P. Glatzel, *J. Electron Spectros. Relat. Phenomena*, 2011, **184**, 210 - 215

88 R. Taylor, S. Coulombe, T. Otanicar, P. Phelan, A. Gunawan, W. Lv, G. Rosengarten, R. Prasher and H. Tyagi, *J. Appl. Phys*, 2013, **113**, 11301.

89 *Colloidal Magnetic Fluids: Basics, Development and Application of ferrofluids*, ed. S. Odenbach, Springer, Berlin Heidelberg, 2009

90 M. Sikora, A. Juhin, T. C. Weng, P. Sainctavit, C. Detlefs, F. De Groot and P. Glatzel, *Phys. Rev. Lett.*, 2010, **105**, 037202.

91 A. Juhin, P. Sainctavit, K. Ollefs, M. Sikora, A. Filipponi, P. Glatzel, F. Wilhelm and A. Rogalev, *J. Phys.: Condens. Matter*, 2016, **28**, 505202.

92 M. Sikora, A. Juhin, G. Simon, M. Zajc, K. Biernacka, C. Kapusta, L. Morellon, M. R. Ibarra and P. Glatzel, in *Journal of Applied Physics*, 2012, **111**, 07E301.

93 A. Juhin, A. López-Ortega, M. Sikora, C. Carvallo, M. Estrader, S. Estradé, F. Peiró, M. D. Baró, P. Sainctavit, P. Glatzel and J. Nogués, *Nanoscale*, 2014, **6**, 11911–11920.

94 N. Daffé, M. Sikora, M. Rovezzi, N. Bouldi, V. Gavrilov, S. Neveu, F. Choueikani, P. Ohresser, V. Dupuis, D. Taverna, A. Gloter, M. A. Arrio, P. Sainctavit and A. Juhin, *Adv. Mater. Interfaces*, 2017, **4**, 1700599.

95 N. Daffé, J. Zečević, K. N. Trohidou, M. Sikora, M. Rovezzi, C. Carvallo, M. Vasilakaki, S. Neveu, J. D. Meeldijk, N. Bouldi, V. Gavrilov, Y. Guyodo, F. Choueikani, V. Dupuis, D. Taverna, P. Sainctavit and A. Juhin, *Nanoscale*, 2020, **12**, 11222–11231.

96 A. Warland, C. Antoniak, M. Darbandi, C. Weis, J. Landers, W. Keune and H. Wende, *Phys. Rev. B: Condens. Matter Mater. Phys.*, 2012, **85**, 235113

97 A. G. Roca, R. Costo, A. F. Rebolledo, S. Veintemillas-Verdaguer, P. Tartaj, T. González-Carreño, M. P. Morales and C. J. Serna, *J. Phys. D. Appl. Phys.*, 2009, **42**, 224002

98 S. Laurent, D. Forge, M. Port, a Roch, C. Robic, L. V Elst and R. N. Muller, *Chem. Rev.*, 2010, **110**, 2574.

99 L. H. Reddy, J. L. Arias, J. Nicolas and P. Couvreur, *Chem. Rev.*, 2012, **112**, 5818–5878.

100 R. A. Revia and M. Zhang, *Mater. Today*, 2016, 19, 157–168.

101 A. C. Anselmo and S. Mitragotri, *AAPS J.*, 2015, **17**, 1041–1054.